Comparison of reconstruction algorithms for optical diffraction tomography

Pengyi Guo and Anthony J. Devaney

Department of Electrical and Computer Engineering, Northeastern University, Boston, Massachusetts 02115

Received November 30, 2004; revised manuscript received April 6, 2005; accepted April 6, 2005

A recently developed inverse scattering algorithm [A. J. Devaney and M. Dennison, Inverse Probl., **19**, 855 (2003) and M. Dennison and A. J. Devaney, Inverse Probl., **20**, 1307 (2004)] is described and applied in a computer simulation study of optical diffraction tomography (ODT). The new algorithm is superior to standard ODT reconstruction algorithms, such as the filtered backpropagation algorithm, in applications employing a limited number of scattering experiments (the so-called limited-view case) and also in cases where multiple scattering occurs between the object being interrogated and the (known) background in which the object is embedded. The new algorithm is compared and contrasted with the filtered backpropagation algorithm in a computer simulation of ODT of weakly inhomogeneous cylindrical objects being interrogated in a limited number of scattering experiments employing incident plane waves. Our study has potential applications in biomedical imaging and tomographic microscopy.

OCIS codes: 110.6960, 290.3200, 100.3010, 100.3190, 100.6950.

1. INTRODUCTION

In optical diffraction tomography (ODT) a semitransparent object is interrogated in a set of scattering experiments employing coherent incident waves, and the amplitude and phase of the resulting scattered optical waves are recorded and used to reconstruct the internal complex index-of-refraction distribution of the object.[1–4] The standard reconstruction algorithms employed in ODT are based on the well-known Born or Rytov approximation[5,6] and require that the object being studied be embedded in a uniform constant-index-of-refraction background medium whose (constant) index of refraction is closely matched to that of the object. In addition, these algorithms are usually based on the so-called generalized projection-slice theorem[5,7] of diffraction tomography (DT), which requires that the experiments employ a large set of incident plane waves whose directions of incidence are closely packed over the unit sphere.

In two recent papers[8,9] a new inverse scattering algorithm was developed that is not based on the generalized projection-slice theorem and that overcomes many of the limitations of the standard DT reconstruction algorithms. This new algorithm is based on the so-called distorted-wave Born approximation[10] and Hilbert-space decomposition[11,12] and allows the object being interrogated to be embedded in a nonuniform background medium and also allows arbitrary incident wave fields to be employed in the set of scattering experiments. Unlike the standard DT reconstruction algorithms such as the filtered backpropagation (FBP) algorithm,[5] this new algorithm also applies to the so-called limited-view problem where the number of scattering experiments is limited. In such cases, it returns a minimum L^2 norm object distribution that is consistent with the scattering data (a pseudoinverse), whereas the standard DT algorithms will generate reconstructions that are not necessarily consistent with the scattering data.

In this paper we adapt the inverse scattering algorithm developed in Refs. 8 and 9 to the case of ODT and test and compare its performance against the standard FBP algorithm in a computer simulation study. We will perform the comparison of the two algorithms only within the Born approximation because the FBP algorithm is based on and is valid only within the Born approximation.[5] The application of the new algorithm to arbitrary source fields and detection geometry within the distorted-wave Born approximation does not serve the comparison purpose and is not discussed in the paper but can be found in Refs. 8 and 9 The paper includes a brief description of the experimental requirements of ODT and suggests the use of phase-shifting holography[13] (PSH) for determining the amplitude and phase of the scattered optical wave fields required by the reconstruction algorithm.

2. OPTICAL DIFFRACTION TOMOGRAPHY

We will employ the standard ODT experimental configuration[1–4] where a semitransparent object is mounted in such a way that it can achieve varying orientations relative to the direction of propagation of an illuminating plane wave as illustrated in Fig. 1. In order to simplify the theory and computer simulations, we will restrict our attention in this paper to the class of cylindrical objects whose properties (index-of-refraction distribution) do not vary along some direction, which we will take to be the z axis of rotation of the rotating mount illustrated in Fig. 2. (In the case of general 3D objects, the mount must rotate about two axes, allowing illumination of the object from all propagation directions over the unit sphere). For any given orientation of the mount, a coherent plane wave whose unit propagation vector $\mathbf{s}$ is perpendicular to the axis of rotation of the mount is incident on the object, and the intensity of the scattered wave field is recorded by the CCD array. In order to reconstruct the object's internal

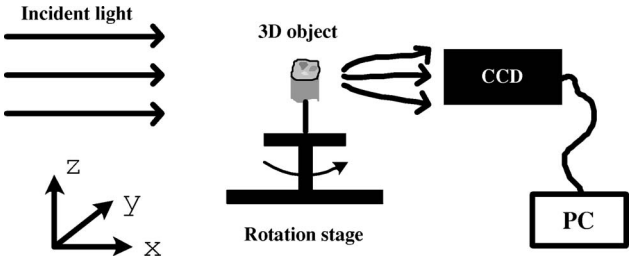

Fig. 1. Optically semitransparent object is mounted in such a way that it can achieve varying orientations relative to the direction of incident light.

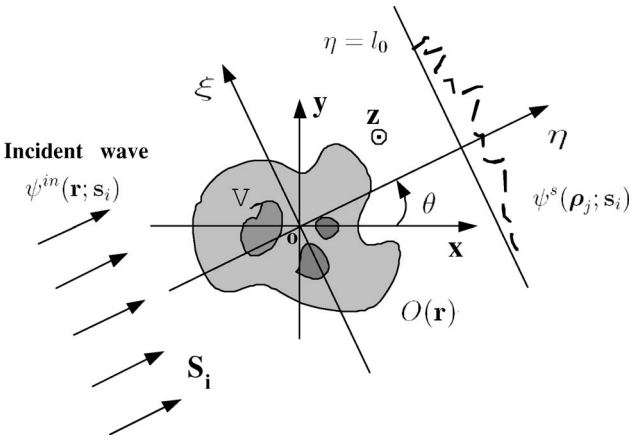

Fig. 2. Mathematic model of DT.

complex index-of-refraction distribution, one needs to determine both the amplitude and the phase of the scattered field from the measured intensity, and in many of the previous studies of ODT this was accomplished via the use of a phase-retrieval algorithm.[14,15] Such algorithms have a number of limitations, however, and an alternative procedure using PSH can also be employed for this purpose and is described in Ref. 13.

In order to accurately determine the internal structure of the object, one needs to perform a number of scattering experiments, using varying angles of illumination of the incident plane wave relative to the object. For cylindrical objects and the system illustrated in Fig. 1, this is accomplished by simply rotating the (cylindrical) object about its axis. We can regard the object as being fixed (nonrotating) in space and the incident plane wave and CCD detector array as rotating around the object with its optical axis (and incident plane-wave direction) defined by the unit vector **s**, which, in the ideal situation, can completely cover the unit circle. For any given relative orientation between the object and the optical axis of the system, the optical scattered wave is then assumed to be determined via phase retrieval or PSH, and the goal of ODT is to determine the internal complex index-of-refraction distribution of the object from such a set of scattered wave field amplitudes.

We note that the success of the reconstruction algorithms of ODT depends on the validity of a weak scattering relationship between the object's index-of-refraction distribution and the scattered field amplitude over the detector array plane. In practice, this is achieved by immersing the object in a test tube or similar structure that is filled with an index-matching fluid. Unfortunately, although this results in weak scattering between the object and the wave propagating in the background index-matching fluid, it also introduces multiple scattering between this background wave and the test tube that can introduce image artifacts into the reconstructed object profile unless accounted for in the ODT reconstruction algorithm. The standard reconstruction algorithms of ODT cannot easily account for these multiple-scattering effects, and one of the primary advantages of the new algorithm to be described here is that it can accommodate such effects.

A. Generalized Projection-Slice Theorem and the Filtered Backpropagation Algorithm

The standard reconstruction algorithms of DT assume incident plane waves and are based on the so-called generalized projection-slice theorem, which, in turn, is based on the first Born or Rytov approximation.[5] In this paper we will restrict our attention to the Born approximation, although much of the development is readily extended to the case of the Rytov approximation without difficulty. The Born approximation results in a linear relationship between the scattered field amplitude and the object's complex index-of-refraction profile. In the case of cylindrical objects illuminated by plane waves propagating perpendicular to their axis of rotation, the index of refraction and resulting scattered field vary only over a plane that, in the experimental system illustrated in Fig. 1, is perpendicular to the axis of rotation of the rotating mount. We define a Cartesian coordinate system whose z axis is aligned along this axis of rotation and whose (x,y) plane is fixed relative to the rotating mount or object. The scattered field amplitude over the CCD array plane will be constant along the z axis and will vary as a function of the ξ coordinate in an (ξ,η,z) Cartesian system that is fixed relative to the CCD array but rotates about the z axis relative to the (x,y,z) system. The geometry is illustrated in Fig. 2.

For cylindrical objects the generalized projection-slice theorem relates the 1D spatial Fourier transform of the scattered field amplitude as determined over the CCD plane to the 2D spatial Fourier transform of the object's complex index-of-refraction distribution. In particular, assuming that the object is embedded in a medium with constant and real wavenumber $k_b=k_0n_b$ (k_0 is free-space wavenumber, and n_b is the refractive index of the background media) and that the incident wave to the object is a plane wave with unit propagation vector **s** lying in the (x,y) plane, then the generalized projection-slice theorem states that

$$\tilde{\psi}(K;l_0) = \frac{ik_0^2n_b}{\gamma}\exp(i\gamma l_0)\tilde{\delta}_n(K,\gamma-K), \tag{1}$$

where $\tilde{\psi}(K;l_0)$ is the spatial Fourier transform of the scattered field at $\eta=l_0$,

$$\gamma = \begin{cases} (k_b^2-K^2)^{1/2}, & K \leqslant k_b \\ i(K^2-k_b^2)^{1/2}, & K > k_b \end{cases}, \tag{2}$$

and

$$\delta n(x,y) = n(x,y) - n_b \tag{3}$$

is the deviation of the object's index-of-refraction profile $n(x,y)$ from the constant index n_b of the uniform background medium and where the tildes denote spatial Fourier transforms.

The generalized projection-slice theorem is the basis for virtually all (quantitative) reconstruction algorithms in DT. Again, we emphasize that its validity depends crucially on the validity of the first Born approximation and also on the requirement that in any given scattering experiment the incident (probing) wave to the scatterer is a single plane wave propagating in the direction defined by the unit vector **s**. In the case where the object is immersed in an index-matching fluid, the theorem will break down owing to the fact that the incident wave is no longer a plane wave but, rather, will be the wave field propagating in the test tube or other structure containing the fluid and object. In past studies of ODT, a rectangular test tube has been employed to minimize these effects. However, even in such cases the effects of undesired multiple scattering in the test tube will be present and will reduce the quality of the object profile reconstructions.

The FBP algorithm[5,16] is derived in a straightforward manner directly from the projection-slice theorem. The algorithm derives its name from the sequence of steps it employs to generate the reconstruction:

- Convolutional filtering of the scattered field data,
- Backpropagation of the filtered data,
- Summation over views,

where each view of the object corresponds to a different incident plane-wave direction **s**. Mathematically, the algorithm is expressed in the form

$$\begin{aligned}\hat{\delta n}(x,y) = \frac{i\exp(-ik_b l_0)}{4\pi k_b}\int_0^{2\pi} d\phi \int_{-k}^{k} dK|K|\tilde{\psi}(K;\phi) \\ \times\exp[i(\gamma - k_b)(x\cos\phi + y\sin\phi - l_0)] \\ \times\exp[iK(y\cos\phi - x\sin\phi)],\end{aligned} \tag{4}$$

where the reconstruction $\hat{\delta n} = (x,y)$ is equal to $\delta n(x,y)$ low pass filtered to the region $|K| \leq \sqrt{2}k_b$. A derivation of the FBP algorithm is presented in Ref. 5, and its computer implementation is presented in Ref. 16.

ODT of weakly scattering objects has been performed by a number of workers. Early work was performed using phase-retrieval techniques[14,15] applied to intensity scans obtained using a scanning photodetector.[1,2] Later work employed a monochrome digital camera and again used phase retrieval to deduce the phase of the optical field from its measured intensity distribution.[4] An excellent example of the use of DT in this class of applications is given in Ref. 3 and is reproduced in the latest edition of Born and Wolf (Ref. 17 page 716).

B. New Algorithm

In this subsection, we specialize the newly developed inverse scattering algorithm reported in Refs. 1 and 2 to the special case of ODT of cylindrical objects using the experimental system illustrated in Fig. 1. Our goal in this paper is to compare the performance of the new algorithm to the standard FBP algorithm,[5] and to do this we will examine the simplest case of a weakly scattering (cylindrical) object embedded in free space where the Born approximation holds. Although the algorithm to be described is applicable to more general and practical situations, the same is not true of the FBP algorithm, and a comparison using these more general scenarios would not serve any purpose.

We employ the same geometry and definitions used above in connection with our discussion of the FBP algorithm. The cylindrical object is located in a fixed (x,y,z) coordinate system whose z axis is aligned along the axis of the object, which is illuminated by an incident plane wave propagating along the $\mathbf{s}_i$ direction. Here, $i = 1,2,\ldots,N_{\mathbf{s}}$; a $\mathbf{s}_i$ is a unit propagation vector lying in the (x,y) plane; and $N_{\mathbf{s}}$ is the number of illuminating directions used in the suite of ODT experiments. For each direction of illumination $\mathbf{s}_i$, we define a rotating coordinate system (ξ,η,z) whose η axis is aligned along the direction of propagation of the illuminating plane wave and whose (ξ,z) plane is parallel to the plane of the CCD array. For each incident wave direction $\mathbf{s}_i$, the scattered wave field is measured by point receivers (CCD pixels) located at $\boldsymbol{\rho}_j = (\xi_j,z)$ on the plane $\eta = l_0$, where $j = 1,2,\ldots,N_{\boldsymbol{\rho}}$; $N_{\boldsymbol{\rho}}$ is the number of point receivers; and l_0 is the fixed distance of the center of the CCD array from the axis of rotation of the rotating mount.

Because the object is cylindrical and the probing plane waves all have propagation vectors lying in the (x,y) plane, the scattered field will be independent of the z coordinate and will depend only on the position vector $\mathbf{r} = (x,y)$. All the scattering equations then become 2D, and, in particular, for each illumination direction $\mathbf{s}_i$ the scattered field at $\boldsymbol{\rho}_j$ can be represented via the Born approximation in the form

$$\begin{aligned}\psi^{(s)}(\boldsymbol{\rho}_j;\mathbf{s}_i) &= \int_V d^2r G_b(\boldsymbol{\rho}_j,\mathbf{r})O(\mathbf{r})\psi^{in}(\mathbf{r};\mathbf{s}_i) \\ &= \int_V d^2r G_b(\boldsymbol{\rho}_j,\mathbf{r})O(\mathbf{r})\exp(ik_b\mathbf{s}_i\cdot\mathbf{r}),\end{aligned} \tag{5}$$

where the integrations in the above equations are taken over the 2D support region V of the object's index-of-refraction profile on the (x,y) plane and where we have defined the object function as

$$O(\mathbf{r}) = k_0^2[n_b^2 - n^2(\mathbf{r})] \cong -2k_0^2 n_b \delta n(\mathbf{r}),$$

with δn as the deviation of the object's index-of refraction profile from the constant index of the background medium n_b [cf. Eq. (3)]. In the above equations $\psi^{in}(\mathbf{r};\mathbf{s}_i) = \exp(ik_b\mathbf{s}_i\cdot\mathbf{r})$ is the incident plane wave, G_b is the 2D background Green function, and k_0 is the free-space wavenumber.

If we define

$$\pi_n(\mathbf{r}) = \begin{cases} G_b^*(\boldsymbol{\rho}_j,\mathbf{r})\exp(-ik_b\mathbf{s}_i\cdot\mathbf{r}), & \text{if } \mathbf{r}\in V \\ 0, & \text{otherwise}\end{cases} \tag{6}$$

and the integral operator as

$$L_n = \int \mathrm{d}^2 r \pi_n^*(\mathbf{r}), \tag{7}$$

where $n=(i-1)N_{\boldsymbol{\rho}}+j$, $i=1,2,\ldots,N_{\mathbf{s}}$, $j=1,2,\ldots,N_{\boldsymbol{\rho}}$, then Eq. (5) can be represented in the form

$$\psi_n^s = \psi^s(\boldsymbol{\rho}_j;\mathbf{s}_i) = L_n O(\mathbf{r}) = \langle \pi_n(\mathbf{r}), O(\mathbf{r})\rangle, \tag{8}$$

where

$$\langle f_1, f_2\rangle = \int \mathrm{d}^2 r f_1^*(\mathbf{r}) f_2(\mathbf{r})$$

is the standard inner product in R^2, i.e., over the (x,y) plane.

Equation (8) states that the scattered field data ψ_n^s is a mathematical projection of the unknown object $O(\mathbf{r})$ onto the functions $\pi_n(\mathbf{r})$, and it is shown in Ref. 8 that this relationship implies that a minimum norm solution for the unknown $O(\mathbf{r})$ can be written in the form of linear combinations of the $\pi_n(\mathbf{r})$ functions; i.e.,

$$\hat{O}(\mathbf{r}) = \sum_{n=1}^{N} C_n \pi_n(\mathbf{r}), \tag{9}$$

where $N=N_{\mathbf{s}}\times N_{\boldsymbol{\rho}}$ and where $\|\hat{O}\|=\langle \hat{O},\hat{O}\rangle^{1/2}$ is minimum among all object functions compactly supported in V. The expansion coefficients C_n are determined by substitution of Eq. (9) into Eq. (8) and are thus required to satisfy the coupled set of linear equations:

$$\psi_n^s = \sum_{m=1}^{N} C_m \langle \pi_n(\mathbf{r}), \pi_m(\mathbf{r})\rangle_V \quad \text{for } n = 1,2,\ldots,N. \tag{10}$$

Equation (10) is a set of N linear equations that can be represented in a matrix form

$$\underline{\underline{A}}\,\underline{c} = \underline{d}, \tag{11}$$

where

$$\underline{c} = (C_1, C_2, \ldots, C_N)^T, \tag{12}$$

$$\underline{d} = (\psi_1^s, \psi_2^s, \ldots, \psi_N^s)^T \tag{13}$$

are column vectors of length N and $\underline{\underline{A}}$ is the N by N constant matrix whose element at the ith row and jth column is determined by

$$\underline{\underline{A}}(ij) = \langle \pi_i(\mathbf{r}), \pi_j(\mathbf{r})\rangle = \int \mathrm{d}^2 r \pi_i^*(\mathbf{r})\pi_j(\mathbf{r}), \tag{14}$$

where $i=1,2,\ldots,N$ and $j=1,2,\ldots,N$. It is easily shown that the matrix $\underline{\underline{A}}$ is Hermitian, i.e., $\underline{\underline{A}}=\underline{\underline{A}}^\dagger$, and hence can be expressed via its eigenvalue decomposition:

$$\underline{\underline{A}} = \underline{\underline{U}}\,\underline{\underline{\Lambda}}\,\underline{\underline{U}}^\dagger, \tag{15}$$

where $\underline{\underline{U}}$ is a N by N unitary matrix and $\underline{\underline{\Lambda}}$ is the N by N diagonal singular-value matrix. The pseudoinverse least-squares solution of Eq. (11) can now be obtained by

$$\hat{c} = \underline{\underline{U}}\,\underline{\underline{\Lambda}}^{-1}\underline{\underline{U}}^\dagger \underline{d}, \tag{16}$$

where $\underline{\underline{\Lambda}}^{-1}$ denotes the diagonal matrix whose nonzero diagonal elements are the reciprocals of the corresponding nonzero diagonal elements of $\underline{\underline{\Lambda}}$.

3. COMPUTER SIMULATION

We simulated an ODT experiment using the new algorithm outlined above and compared its performance with the FBP algorithm. For illustration purposes, we consider a cylindrical object whose index of refraction varies only over the (x,y) plane and where the data are measured at $(\xi_j, \eta=l_0)$ in the rotary (ξ,η) coordinate system. The source was taken to be a He–Ne laser with wavelength $\lambda=633$ nm.

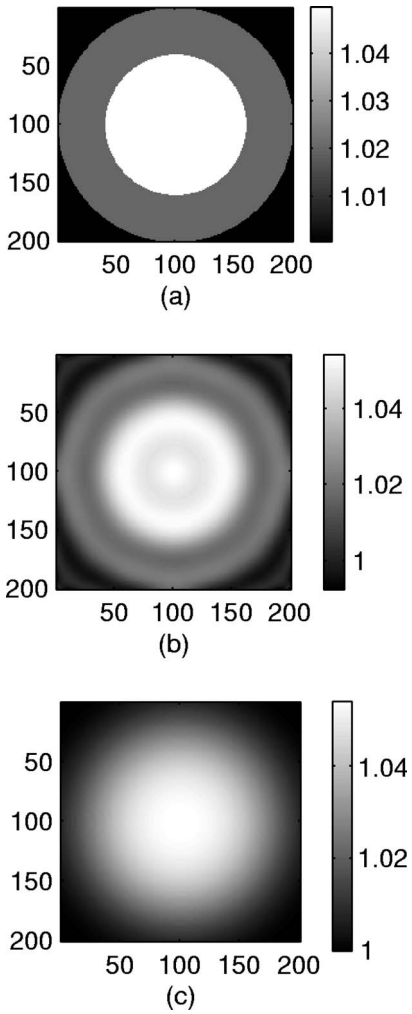

Fig. 3. Cross-sectional images of an optical fiber's refractive-index distribution. (a) Actual cross-sectional refractive index of an optical fiber. (b) Reconstruction of the refractive index of the optical fiber using the new algorithm. (c) Reconstruction of the refractive index of the optical fiber using the FBP algorithm. Pixel size in (a)–(c) is $\delta x=\lambda=633$ nm. The following parameters have been used for reconstruction: measurement distance $l_0 \approx 40$ mm, $N_{\mathbf{s}}=16$ views, $N_\xi=41$ CCD pixels per view, and distance between adjacent CCD pixels $d=26.8$ μm.

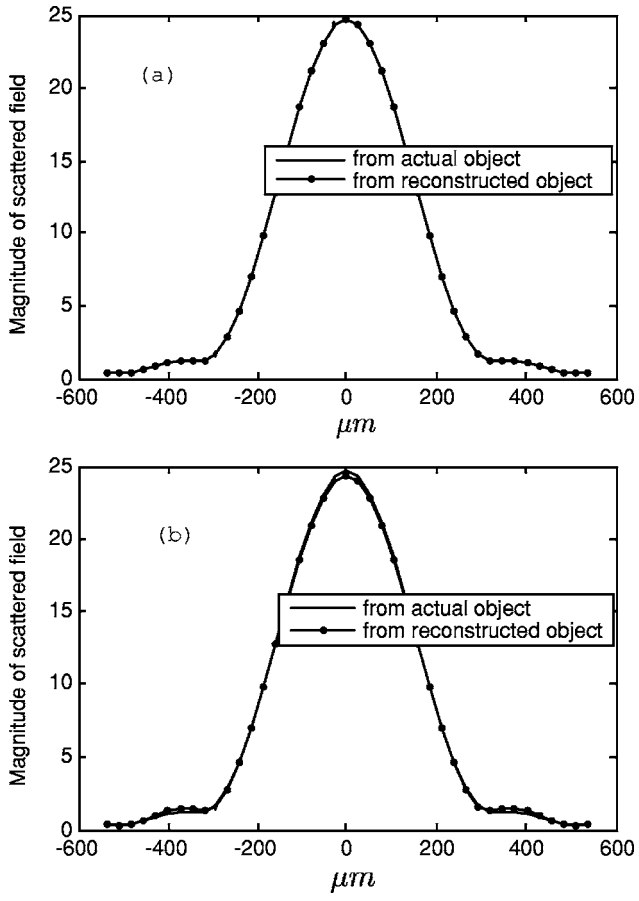

Fig. 4. (a) Comparison of the scattered data (solid curve) generated by the actual object (optical fiber) and the scattered data (dot curve) generated by the reconstructed object that were obtained by the new algorithm. (b) Comparison of the scattered data (solid curve) generated by the actual object (optical fiber) and the scattered data (dot curve) generated by the reconstructed object that were obtained by the FBP algorithm.

A. Limited Data

We first tested the reconstruction of a cylindrical fiber whose cross-sectional refractive-index distribution is given in Fig. 3(a). The object was represented by a 201 $\times 201$ square matrix with a sampling distance $\delta x = \lambda$. Therefore, the object's size was about 127 μm (diameter). The synthetic data were generated using the Born approximation at $l_0 = 63191\lambda \approx 40$ mm. $N_\xi = 41$ CCD pixels (detectors) were placed symmetrically about the η axis and on the line $\eta = l_0$ for each illumination direction $\mathbf{S}_i$. The distance between adjacent CCD pixels was $d = 26.8$ μm. A total of $N_\mathbf{s} = 16$ illumination directions, which were uniformly distributed in the 2π region, were used.

The results from the simulated experiment using the above parameters obtained using the new algorithm and the FBP algorithm are shown in Figs. 3(b) and 3(c), respectively. The figures show that the reconstruction from the new algorithm agrees roughly with the actual object image, although very limited data were used for reconstruction. In particular, only 16 views and 41 pixels per view were employed in this case, and the data were measured at a very large distance (40 mm). The limited data result in distortions and low resolution in the reconstruction as evidenced in the figure. The reconstruction from the FBP algorithm using the same experimental parameters loses much information about the cross-sectional structure of the optical fiber and does not clearly show the core and cladding structure of the fiber.

The reconstructed object was then used in the forward model with the same parameters as discussed above to generate the scattered data, which were then compared with the scattered data that were generated by the actual object. The scattered data for a single view are compared in Figs. 4(a) and 4(b) where the dot curve in Fig. 4(a) represents the scattered data from the reconstructed object obtained using the new algorithm, the dot curve in Fig. 4(b) represents the scattered data from the FBP-reconstructed object, and the solid curves in both figures represent the scattered data from the actual object. The figures show that the reconstructed object by the new algorithm generates scattered field data that agree very well with the actual scattered data and that the reconstructed object by the FBP algorithm generates scattered field data that do not agree with the actual scattered field data. In this sense, the new algorithm is superior to the

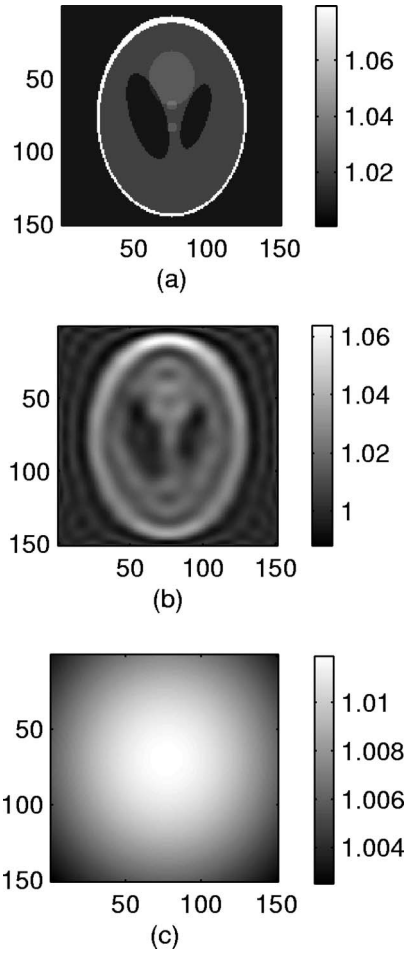

Fig. 5. Reconstruction of a phantom with sparse (limited) data. (a) Actual index of refraction of the phantom. (b) Reconstruction of the refractive index of the phantom using the new algorithm. (c) Reconstruction of the refractive index of the phantom using the FBP algorithm. Pixel size in (a)–(c) is $\delta x = \lambda = 633$ nm. The following parameters have been used for reconstruction: measurement distance $l_0 \approx 45$ mm, $N_\mathbf{s} = 40$ views, $N_\xi = 61$ CCD pixels per view, and distance between adjacent CCD pixels $d = 67$ μm.

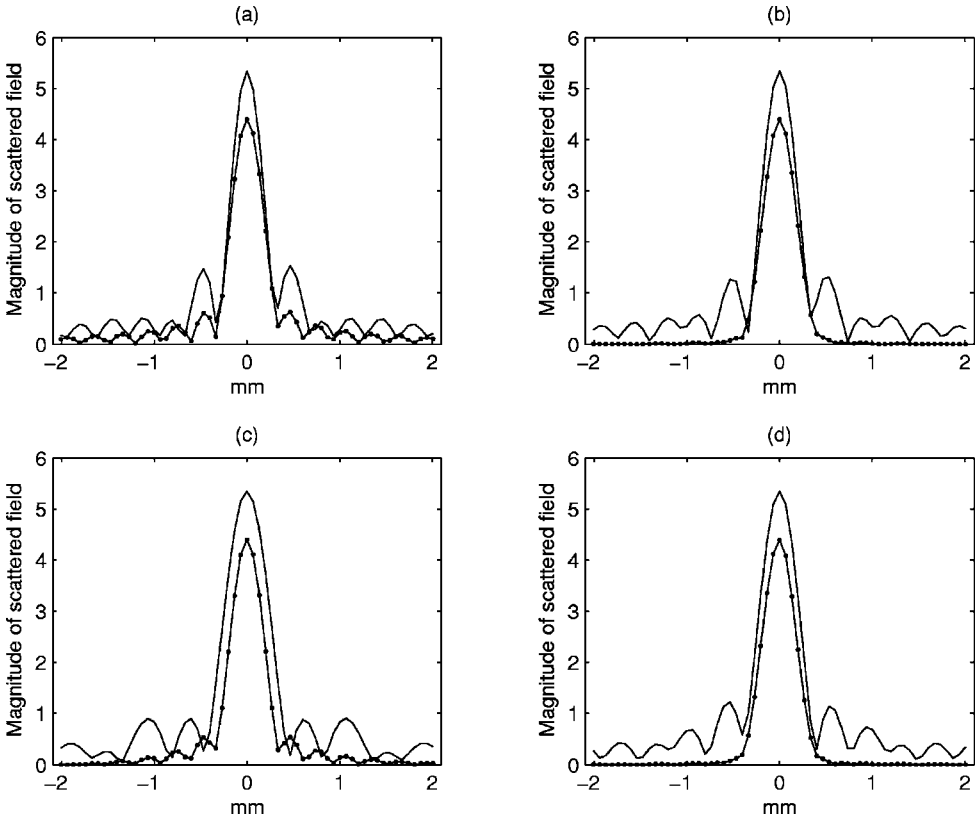

Fig. 6. Comparison of the scattered data (solid curve) generated by the actual object (phantom) and the scattered data generated by the reconstructed object obtained using the FBP algorithm (dotted curve) and the new algorithm (represented by the dashed curve, which agrees with the solid curve). (a)–(d) show the scattered data for four different view angles, respectively.

FBP algorithm in that it yields reconstructions that agree with the data in the limited-view problem.

In the second example, we used a more complicated phantom as our object to test the reconstruction algorithms. In this case, the object was represented by a 150 $\times 150$ matrix with sampling distance $\delta x = \lambda = 633$ nm. The object's size was about 90 μm, and its refractive-index distribution is shown in Fig. 5(a). We followed the same procedure as in the optical fiber example and chose the experimental parameters to be $l_0 = 71090\lambda \approx 45$ mm, $N_\xi = 61$, $d = 67$ μm, and $N_\mathbf{s} = 40$. The reconstructions using two algorithms are shown in Figs. 5(b) and 5(c). In this case, as in the last example, the FBP algorithm fails to accurately reconstruct the object from the sparse data resulting from the limited number of CCD pixels and large distance between adjacent pixels. However, the new algorithm can still produce a fairly good reconstruction with such limited data.

We followed the same procedure as in the optical fiber example to generate the scattered field data by replacing the actual object with the reconstructed object in the forward model. But in this case we compare the data for four different view angles. The scattered field data from the reconstructed object obtained by the new algorithm are plotted as the dashed curve in Fig. 6 and coincide with the scattered field data (solid curve) generated from the actual object. The scattered field data from the reconstructed object by the FBP algorithm are shown as the dotted curve in Fig. 6 and are not consistent with the actual data. In both figures, plots (a)–(d) correspond to the scattered field data for four different view angles, respectively.

B. Dense Data

We employed the same phantom used in the previous example but with much denser data. In particular, we let $l_0 = 301\lambda \approx 190$ μm, $N_\xi = 61$, $d = 1.9$ μm, and $N_\mathbf{s} = 40$. The reconstructions using the new method and the FBP algorithm are shown in Figs. 7(b) and 7(c), respectively. In this case, both reconstruction algorithms are seen to yield almost identical reconstructions. This is due to the fact that the FBP algorithm yields a pseudoinverse in the case of dense data.[5,16]

C. Point-Spread Function

The point-spread function (PSF) is a useful tool to compare the performance of the two algorithms. The PSF of an algorithm is defined as the reconstruction of a point scatterer and is a function of the scattering geometry as well as the location of the point scatterer. In our experiment we computed the reconstruction image of a point scatterer located at the center of a supporting area that is $16\lambda \times 16\lambda$ in size and sampled at a rate of $\delta x = \lambda/8$. The CCD camera was placed 100λ away from the supporting area center, and 401 pixels separated λ from one another were employed. The spectrum of the PSF is approximated by the 2D Fourier transform of the reconstruction images. Each Ewald circle on the spectrum corresponds to the

data collected from one incident angle. For simplicity and illustration purposes, only one incident angle is considered in this experiment. The results were illustrated by Fig. 8, and it is seen that a sharper image and a more complete Ewald circle were obtained by the new method than by the FBP algorithm.

D. Noise

In this subsection we examine the effect of noise on the FBP algorithm and the new algorithm. The first example employed the same object and parameters as those in the ODT reconstruction of an optical fiber described previously and shown in Fig. 9(a). The experimental parameters are as follows.

- Measurement distance $l_0=40$ mm,
- $N_{\mathbf{s}}=16$ views,
- $N_{\xi}=41$ CCD pixels/view,
- Distance between CCD pixels$=26.8$ μm.

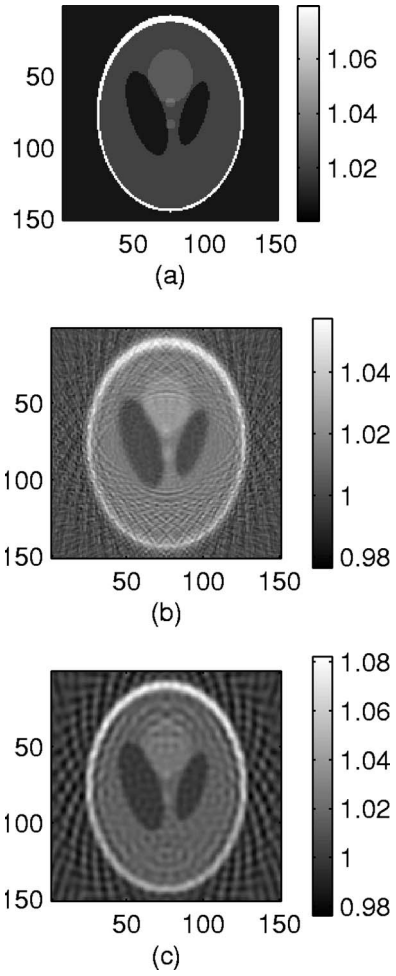

Fig. 7. Reconstruction of a phantom with dense data. (a) Actual index of refraction of a phantom. (b) Reconstruction of the refractive index of the phantom using the new algorithm. (c) Reconstruction of the refractive index of the phantom using the FBP algorithm. Pixel size in (a)–(c) is $\delta x=\lambda=633$ nm. The following parameters have been used for reconstruction: measurement distance $l_0\approx 190$ μm, $N_{\mathbf{s}}=40$ views, $N_{\xi}=61$ CCD pixels per view, and distance between adjacent CCD pixels $d=1.9$ μm.

We first generate the object's scattered field data using the Born approximation as before and then add Gaussian noise to the scattered data with a signal-to-noise ratio (SNR) of 20 dB (i.e., $|\psi|^2/\sigma^2=100$, where ψ is the scattered field and σ^2 is the variance of the Gaussian noise). The DT reconstruction from the noisy scattered field data using the new algorithm is shown in Fig. 9(c). The reconstruction is seen to be very poor owing to the noise that dominates the reconstruction at small values of the eigenvalues of the A matrix defined in Eq. (15). To regularize the inversion, we truncated the eigenvalue spectrum and obtained the result shown in Fig. 9(d). The reconstruction from noise-free scattered field data is also given in Fig. 9(b) for comparison purposes.

In a second example we used the phantom shown in Fig. 7(a) and the following experimental parameters.

- Measurement distance $l_0=190$ μm,
- $N_{\mathbf{s}}=40$ views,
- $N_{\xi}=61$ CCD pixels per view,
- Distance between CCD pixels$=1.9$ μm.

We followed the same procedure as in the previous example to generate the synthetic data and reconstructions from the noise-free and noisy synthetic data. The reconstructions from noisy scattered data (SNR$=20$ dB) by the new and FBP algorithms are shown in Figs. 10(c) and 10(e), respectively. We can see that in this case the new algorithm is more sensitive to the noise than the FBP algorithm. We then truncated the eigenvalue spectrum in the new algorithm and obtained the reconstruction shown in Fig. 10(d). The reconstructions by the new algorithm and the FBP algorithm from noise-free data are also given in Fig. 10(a) and 10(b), respectively, for comparison purposes.

4. DISCUSSION AND CONCLUSIONS

In this paper, a new optical diffraction tomography (ODT) reconstruction algorithm is introduced and compared with the standard FBP algorithm within the Born approximation. The new algorithm generates a least-squares psuedoinverse of the object from scattered field data measurements in the form of a series of products of complex-conjugate background Green functions whose expansion coefficients are readily found by inverting a set of N simultaneous linear algebraic equations with N unknowns. A key feature of this algorithm is its ability to reconstruct the object profile with limited data. In addition, the algorithm is computationally efficient and is easily regularized so as to be stable in the presence of noise. Examples of the reconstruction using the two algorithms have been presented to compare their imaging performance. Another interesting aspect of this algorithm is the limited-view problem where the range of view angles is restricted. Because this algorithm can use the distorted-wave Born approximation, reflection from known boundaries can be exploited to essentially expand the range of views and hence to improve the reconstruction quality.[8,9]

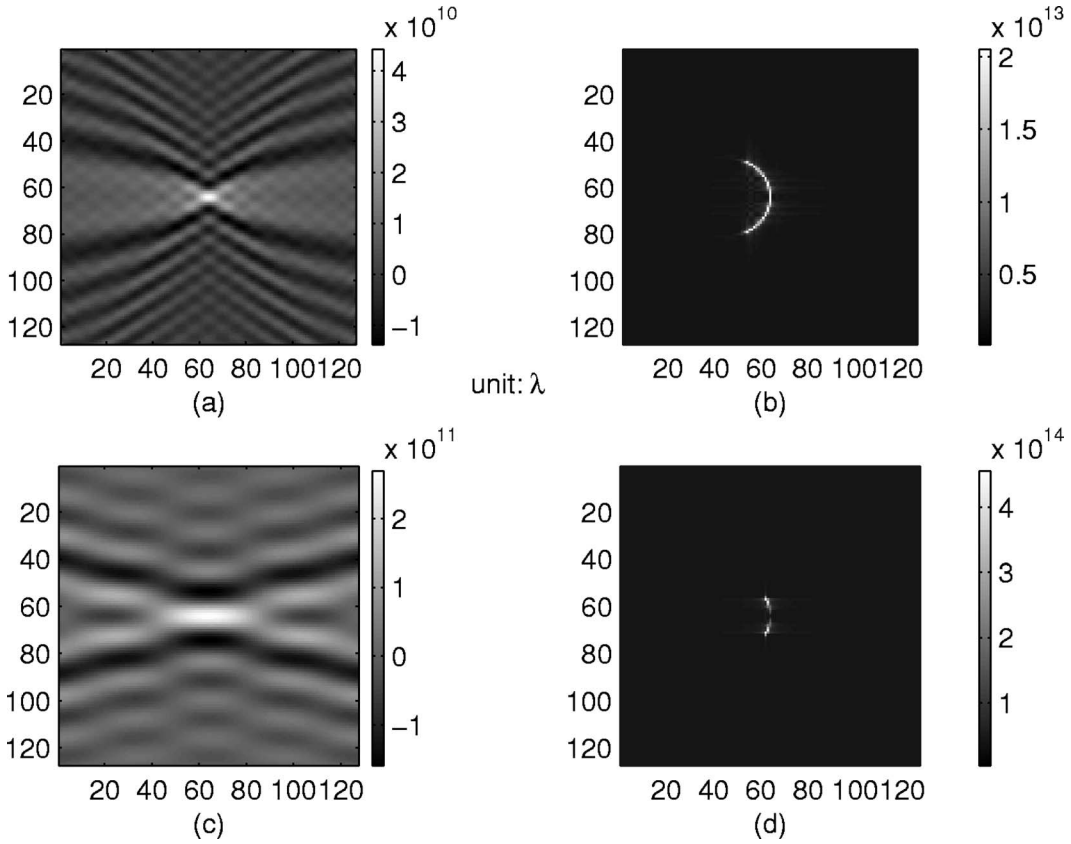

Fig. 8. Comparison of PSFs between the new and the FBP algorithms. (a) Real part of the reconstructed point scatter by the new algorithm. (b) Spectrum of the new algorithm PSF. (c) Real part of the reconstructed point scatter by the FBP algorithm. (d) Spectrum of the FBP algorithm PSF.

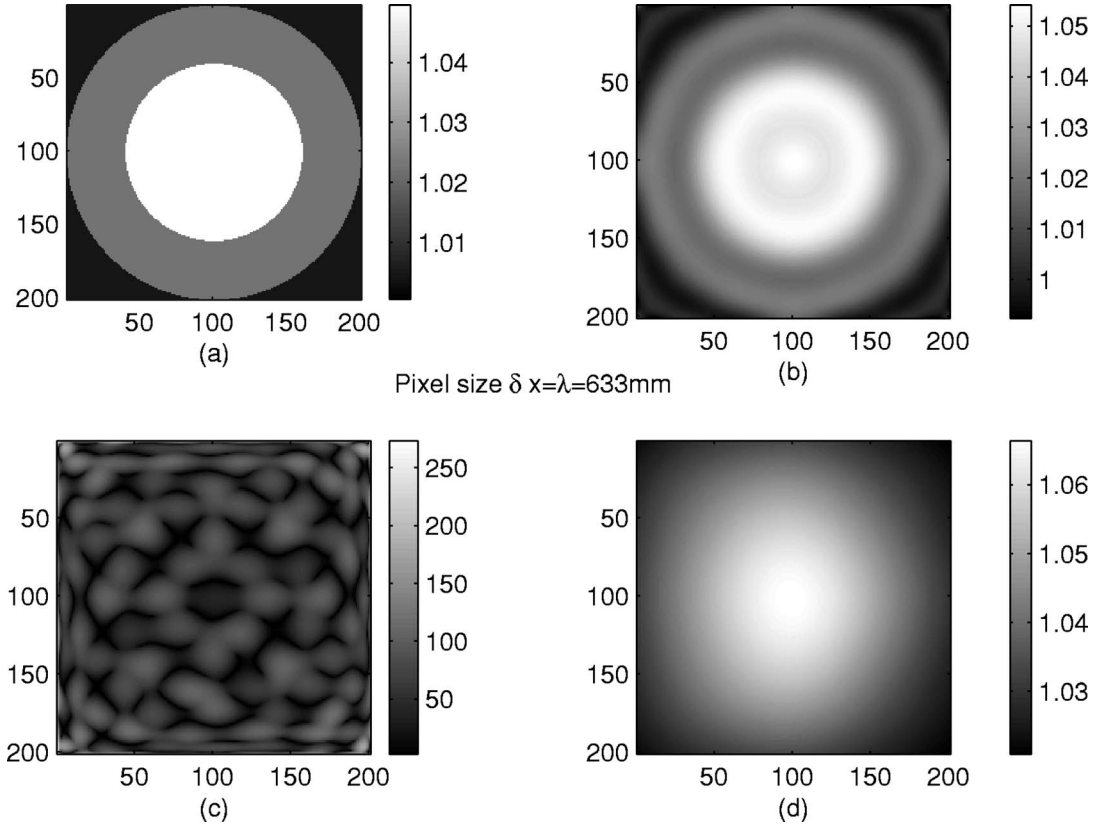

Fig. 9. Reconstructions by the new algorithm. (a) Object. (b) Reconstruction by the new algorithm from noise-free scattered data. (c) Reconstruction by the new algorithm from noisy data [Signal-to-noise ratio (SNR)=20 dB]. (d) Reconstruction by the new algorithm using a truncated eigenvalue spectrum with noisy data (SNR=20 dB).

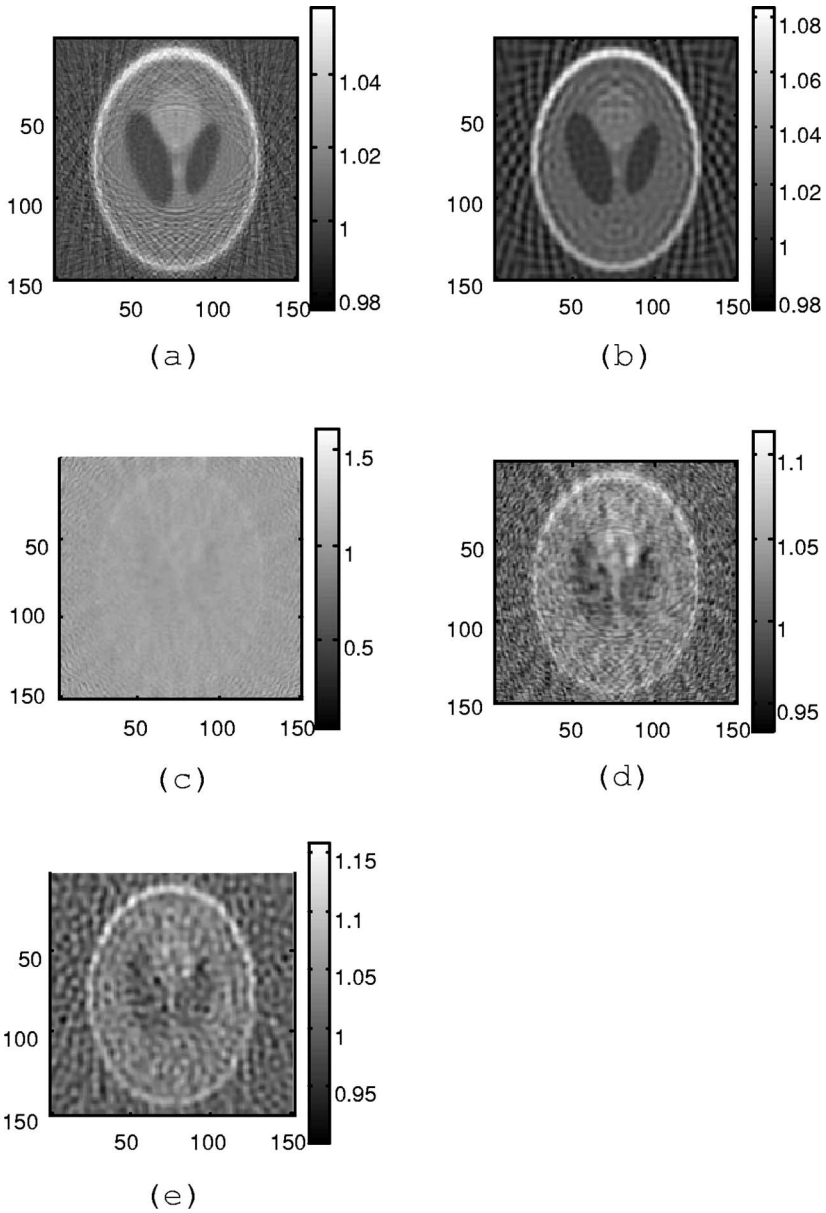

Fig. 10. Reconstructions with noisy data. (a) Reconstruction by the new algorithm from noise-free scattered data. (b) Reconstruction by the FBP algorithm from noise-free scattered data. (c) Reconstruction by the new algorithm from noisy data (SNR=20 dB) without using a truncated eigenvalue spectrum. (d) Reconstruction by the new algorithm using a truncated eigenvalue spectrum with noisy data (SNR=20 dB). (e) Reconstruction by the FBP algorithm with noisy data (SNR=20 dB). Pixel size in (a)–(e) is $\delta x = \lambda = 633$ nm.

Authors A. J. Devaney and P. Guo can be reached by e-mail at devaney@ece.neu.edu and p.guo@duke.edu, respectively.

REFERENCES

1. A. J. Devaney, M. Maleki, and A. Schatzberg, "Tomographic reconstruction from optical scattered intensities," J. Opt. Soc. Am. A **9**, 1356–1363 (1992).
2. T. C. Wedberg and J. J. Stamnes, "Experimental examination of the quantitative imaging properties of optical diffraction tomography," J. Opt. Soc. Am. A **12**, 493–500 (1995).
3. T. C. Wedberg and W. C. Wedberg, "Tomographic reconstruction of the cross-sectional complex refractive index of semitransparent, birefringent fibers," J. Microsc. **177**, 53–67 (1995).
4. M. Maleki and A. J. Devaney, "Phase retrieval and intensity-only reconstruction algorithm for optical diffraction tomography," J. Opt. Soc. Am. A **10**, 1086–1092 (1993).
5. A. J. Devaney, "A filtered backpropagation algorithm for diffraction tomography," Ultrason. Imaging **4**, 336–350 (1982).
6. A. J. Devaney, "Geophysical diffraction tomography," IEEE Trans. Geosci. Remote Sens. GE-**22**, 3–12 (1984).
7. A. C. Kak and M. Slaney, *Principles of Computerized Tomographic Imaging* (IEEE, 1988).
8. A. J. Devaney and M. Dennison, "Inverse scattering in inhomogeneous background media," Inverse Probl. **19**, 855–870 (2003).
9. M. Dennison and A. J. Devaney, "Inverse scattering in inhomogeneous background media: II. Multi-frequency case and SVD formulation," Inverse Probl. **20**, 1307–1324 (2004).

10. J. H. Taylor, *Scattering Theory* (Wiley, 1972).
11. T. J. Hall, A. M. Darling, and M. A. Fiddy, "Image compression and restoration incorporating prior knowledge," Opt. Lett. **7**, 467–468 (1982).
12. C. L. Byme, R. M. Fitzgerald, M. A. Fiddy, T. J. Hall, and A. M. Darling, "Image restoration and resolution enhancement," J. Opt. Soc. Am. **73**, 1481–1487 (1983).
13. P. Guo and A. J. Devaney, "Digital microscopy using phase-shifting digital holography with two reference waves," Opt. Lett. **29**, 857–859 (2004).
14. R. W. Gerchberg and W. O. Saxton, "A practical algorithm for the determination of phase from image and diffraction phase pictures," Optik (Stuttgart) **35**, 237–246 (1972).
15. R. A. Gonsalves, "Phase retrieval from modulus data," J. Opt. Soc. Am. **66**, 961–964 (1976).
16. A. J. Devaney, "A computer simulation study of diffraction tomography," IEEE Trans. Biomed. Eng. **30**, 377–386 (1983).
17. M. Born and E. Wolf, *Principles of Optics* (Cambridge U. Press, Cambridge, UK, 1999).